Marine redox conditions in the middle Proterozoic ocean and isotopic constraints on authigenic carbonate formation: Insights from the Chuanlinggou Formation, Yanshan Basin, North China

Chao Li [a,*], Noah J. Planavsky [b], Gordon D. Love [c], Christopher T. Reinhard [d], Dalton Hardisty [c], Lianjun Feng [e], Steven M. Bates [c], Jing Huang [f], Qirui Zhang [e], Xuelei Chu [e], Timothy W. Lyons [c]

[a] *State Key Laboratory of Biogeology and Environmental Geology, China University of Geosciences, Wuhan 430074, China*
[b] *Department of Geology and Geophysics, Yale University, New Haven, CT 06520, USA*
[c] *Department of Earth Sciences, University of California, Riverside, CA 92521, USA*
[d] *School of Earth and Atmospheric Sciences, Georgia Institute of Technology, Atlanta, GA 30332, USA*
[e] *Institute of Geology and Geophysics, Chinese Academy of Sciences, Beijing 100029, China*
[f] *CAS Key Laboratory of Crust-Mantle Materials and Environments, School of Earth and Space Science, University of Science and Technology of China, Hefei 230026, China*

Abstract

To improve our understanding of ocean chemistry and biogeochemical cycling following the termination of large-scale Paleoproterozoic iron formation (IF) deposition (∼1.85 billion years ago [Ga]), we conducted a Fe–S–C–Mo geochemical study of the ∼1.65 Ga Chuanlinggou Formation, Yanshan Basin, North China. Despite the cessation of IF deposition, our results suggest the presence of anoxic but non-euxinic (ferruginous) conditions persisted below the surface mixed layer for the deepest portion of the continental rifting basin and that this pattern is apparently independent of the local organic carbon content. However, our paired S-isotope data of carbonate-associated sulfate and pyrite suggest presence of sulfate in pore fluids, which is not consistent with insufficient sulfate for bacterial sulfate reduction in the water column. Despite evidence for deposition under anoxic conditions, sedimentary molybdenum (Mo) concentrations are mostly not enriched relative to average continental crust. This relationship is consistent with the notion that sulfide-dominated conditions in the water column and/or the sediments are required for Mo enrichment and validates past assertions that Mo enrichment patterns in ancient shales track both the local presence *and* global distribution of euxinia specifically. In addition, we identified extensive diagenetic carbonate precipitation in the upper Chuanlinggou Formation with only moderately negative $\delta^{13}C$ values ($-3.4 \pm 1.4‰$). We propose, with support from a numerical model, that these diagenetic carbon isotope values were most likely derived from precipitation of carbonates dominantly in the methanic zone within the sediments. Diagenetic carbonate precipitation in the methanic zone is likely to have been more extensive in the Proterozoic than the Phanerozoic due to porewater oxidant limitation.

---

* Corresponding author. Tel.: +86 27 67883606.
  E-mail address: chaoli@cug.edu.cn (C. Li).

1. INTRODUCTION

The last episode of major, economic iron formation (IF) deposition occurred around 1.85 Ga. Traditionally, this transition in the sedimentary record was linked to a shift from an anoxic and Fe-rich (ferruginous) ocean to one with mildly oxic deep waters (Holland, 2006; Slack et al., 2007, 2009). However, because H_2S can also titrate dissolved Fe^{2+} in anoxic marine environments to form pyrite, the global development of euxinic conditions in the deep ocean has been suggested as being responsible for the disappearance of large IFs at ~1.85 Ga (Wilde, 1987; Canfield, 1998; Poulton et al., 2004). Indeed, multiple lines of evidence point to widespread euxinia in the mid-Proterozoic ocean (e.g., Shen et al., 2003; Brocks et al., 2005; Scott et al., 2008). Following from this model, delayed eukaryotic expansion and diversification in mid-Proterozoic oceans has been attributed to the limited availability of bioessential and redox-sensitive metals (e.g., Fe, Mo, Cu, Zn, Cd) that could be readily removed from sulfidic waters (e.g., Anbar and Knoll, 2002; Scott et al., 2008; Reinhard et al., 2013).

Rather than global-scale deep euxinia, recent studies have proposed that Proterozoic ocean waters below the surface mixed layer remained largely ferruginous (Canfield et al., 2008; Li et al., 2010; Poulton et al., 2010; Poulton and Canfield, 2011; Planavsky et al., 2011; Reinhard et al., 2013), although oxic deep waters may have prevailed in some oligotrophic basins (e.g., Sperling et al., 2014). Further, there is evidence that productive ocean margin settings were commonly characterized by mid-depth euxinia with surface, at least weakly oxic waters and deeper ferruginous waters (Li et al., 2010, 2012; Poulton et al., 2010; Poulton and Canfield, 2011; reviewed in Lyons et al., 2012, 2014). Euxinia in the Proterozoic oceans spatially limited to intermediate depths, dominantly on ocean margins, may still have been sufficient to terminate the deposition of the large IF at ~1.85 Ga (e.g., Poulton et al., 2010; Kendall et al., 2011). Alternatively, the end of major IF deposition may have been linked to changes in hydrothermal fluid Fe-to-sulfide ratios (e.g., Kump and Seyfried, 2005; Planavsky et al., 2011) and the overall fluxes of those fluids to the ocean (Isley and Abbott, 1999; Bekker et al., 2010). More generally, expanding euxinia on the continental margin may have been a factor leading to the patchy temporal record of early metazoan fossils (and inferred diversification rates) in the late Neoproterozoic (e.g., Li et al., 2010) and the early Cambrian (Feng et al., 2014; Jin et al., 2014), as well as to the mass extinctions at the end-Ordovician (Hammarlund et al., 2012) and end-Permian (e.g., Algeo et al., 2011), among others, suggesting a close relationship between the spatial patterns of marine euxinia and ecosystem stability through Earth history.

In order to investigate Proterozoic ocean chemistry during a key transitional period—the late Paleoproterozoic—and specifically to probe the nature of ocean redox structure, we conducted a Fe–S–C–Mo biogeochemical study of the ~1.65 Ga Chuanlinggou Formation in the late Paleoproterozoic semi-restricted continental rifting Yanshan Basin, North China. In this study, we aim to address two themes: (1) reconstructing seawater chemistry in a continental rift basin and (2) the overarching factors that controlled seawater chemistry in the basin and in turn the broader implications for global ocean chemistry during the mid-Proterozoic.

2. GEOLOGIC BACKGROUND

2.1. Tectonics, stratigraphy, and paleogeography

The Yanshan Basin was a continental rift setting that developed within the northern margin of the North China Block (Fig. 1A) between ~1.8 and 1.6 Ga. This continental rifting was possibly linked to the early partial breakup of the supercontinent Columbia (also known as Nuna) in the mid-Proterozoic from 1.6 to 1.2 Ga (Kusky and Li, 2003; Meng et al., 2011; Zhang et al., 2012, and references therein). The Changcheng Group is the earliest stratigraphic unit in the basin and consists of the Changzhougou, Chuanlinggou, Tuanshanzi, and Dahongyu formations (Fig. 1B). The Changcheng Group is distributed mainly in relatively narrow fault-bounded zones of apparent graben and half-graben geometries (Fig. 1A; Yan and Liu, 1998; Qiao and Gao, 2007).

In the depocenter area at Jixian, the basic geology of the Proterozoic succession, including the Changcheng Group, has been studied systematically (e.g., Chen et al., 1980). The Changzhougou Formation, which unconformably overlies an Archean metamorphic complex, was dominated by fluvial coarse sandstones and conglomerates in its lower portion and by littoral-intertidal siltstones and sandstones in its upper portion. Inferences of a predominantly fluvial-littoral-intertidal depositional environment are supported by abundant wave- and current-generated sedimentary structures, such as ripples, swash marks, and cross bedding in the formation (Fig. 1B). The lower Chuanlinggou Formation consists mainly of silty illitic shales with interbedded siltstones/sandstones and is characterized by sedimentary structures, such as cross bedding, indicative of a shallow marine environment. The middle Chuanlinggou Formation is mainly composed of black illitic shales with clear planar bedding, suggesting a subtidal low-energy environment during deposition. The upper Chuanlinggou Formation consists mainly of calcareous black shales that are intercalated with early- to mid-stage diagenetic carbonate beds, nodules, lenses and laminae (Fig. 2). The diagenetic carbonate laminae, lenses and nodules are typically bedding-parallel with a wide range of lengths from a less than centimeters to almost 50 cm. Diagenetic beds/laminae/lenses/nodules can be characterized by gradual and irregular, wavy boundaries—similar to those commonly observed in Phanerozoic successions that have received extensive study (e.g., Miocene Monterey Formation, Loyd et al., 2012). Some small carbonate veins penetrate the black shale layers with wrinkles and are often terminated by bedding-parallel carbonate beds or laminae (Fig. 2D); these features are similar to those sand veins and microbially induced sedimentary structures (MISS) previously found in the middle Chuanlinggou Formation (Shi et al., 2008), thus well consistent with their diagenetic origins. Some silty
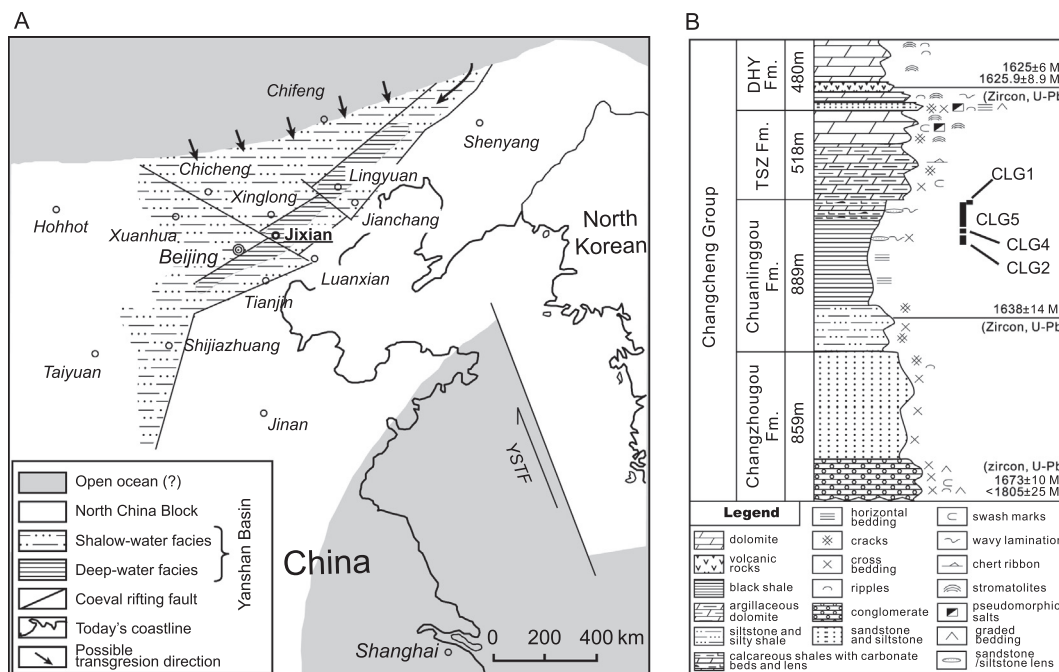
Fig. 1. Geological background for the 1.65 Ga Chuanlinggou Formation. (A) Tectonic and paleogeographic context for the Yanshan Basin during the deposition of the Chuanlinggou Formation (after Qiao and Gao, 2007, and Yan and Liu, 1998). YSTF: Yellow Sea Transform Fault. Arrows represent invasion of open ocean water into the basin from an N and NE direction during the marine transgression as recorded in the middle Chuanlinggou Formation. (B) Generalized stratigraphic column with detailed sedimentary structures of the Changcheng System at the Jixian section (after Chen et al., 1980 and Chu et al., 2007). Age data sources: Lu and Li (1991), Wan et al. (2003), Gao et al. (2008, 2009), Li et al. (2011). Formations: TSZ (Tuanshanzi); DHY (Dahongyu). CLG1, CLG2, CLG4 and CLG5 are the outcrop subsections at the Jixian section.
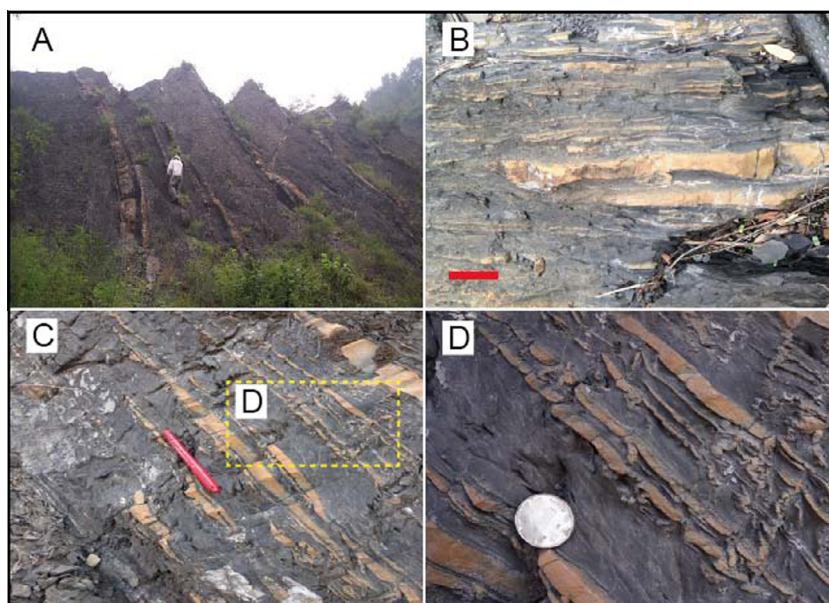

Fig. 2. Diagenetic carbonate beds, nodules, lenses and laminae within the calcareous black shale facies of the upper Chuanlinggou Formation at the Jixian section. (A) A view of the upper subsection CLG5 showing carbonate beds. (B and C) Typical carbonate nodules, lenses and laminae within the calcareous black shales. The red bar in B and the red marker pen in C are 5 cm and ∼15 cm, respectively, for scale. (D) A close look of the diagenetic carbonates in the dashed yellow frame in C showing perpendicular-to-high angle veins (to bedding layers) with wrinkles and wavy boundaries. The coin in D is 2.5 cm in diameter for scale.

beds and lenses with relatively high-energy sedimentary structures have been found locally in the middle-to-upper Chuanlinggou Formation (Fig. 1), suggesting shoaling during deposition. Therefore, the middle-to-upper Chuanlinggou Formation was most likely deposited in a predominantly subtidal environment with episodic shoaling into an intertidal environment.

The overlying Tuanshanzi Formation is dominantly composed of muddy dolostones in the lower portion and stromatolitic dolostones in the upper portion, which are locally intercalated with siltstone or silty shale beds; abundant sedimentary structures such as mud cracks and cross bedding were found in the formation, indicating an intertidal to supratidal/lagoonal environment (Fig. 1B). Thus, the Changcheng Group is typically interpreted as recording a transgressive–regressive cycle in its first three formations, with peak transgression coincident with deposition of the black shales of the Chuanlinggou Formation (Yan and Liu, 1998).

The Chuanlinggou Formation shows a basin-scale water depth gradient running from north to south with deepwater facies deposited in the south along a narrow belt bounded by two sets of NE- to SW-trending rift faults (Beijing–Lingyuan and Luanxian–Jianchang in Fig. 1A). During the transgressive phase of deposition for the Chuanlinggou Formation, open ocean waters likely flowed into the basin from the north (Qiao, 2002), the northeast (Yan and Liu, 1998), or both, and a water-depth gradient developed from the north to the rift zone (Fig. 1A). Such a depth gradient has been clearly identified in the transitional Xinglong area (Xu et al., 2002). Therefore, the Yanshan Basin was generally a semi-restricted rift basin during deposition of the Chuanlinggou Formation, with maximum connection to the open ocean at the time of the peak transgression.

Our samples were collected from the Chuanlinggou Formation in the depocenter area at Jixian from four outcrop subsections (CLG1, CLG2, CLG4, and CLG5 in Fig. 1B). These comprise the middle to upper Chuanlinggou Formation in a section with a general lithologic transition from silty black shales to calcareous black shales (Fig. 1B). The calcareous black shales without any evidence for high-energy depositional conditions (CLG-5) are interpreted as the deepest facies. These subtidal black shales represent water depths beneath storm wave base from the deepest portion of the Yanshan basin—but are certainly not considered 'deep' in an open ocean sense.

2.2. Chronology

Zircon U–Pb ages of 1625 ± 6 million years (Ma) (Lu and Li, 1991) and 1625.9 ± 8.9 Ma (Gao et al., 2008) from the Dahongyu volcanic rocks in the Jixian area and the youngest U–Pb age of 1805 ± 25 Ma from the Changzhougou detrital zircons in the Beijing area (Wan et al., 2003) place the age of the Changcheng Group in the range of ca. 1.8–1.6 Ga. Recently, the age model for deposition of sedimentary strata within the Changcheng Group was revised to 1.7–1.6 Ga to be consistent with new U–Pb volcanic ages of 1673 ± 10 Ma for a granite-porphyry dike

(Li et al., 2011) and 1731 ± 4 Ma for a mafic dike (Peng et al., 2012). These dikes were emplaced into the Archean metamorphic basement but were unconformably overlain by the Changzhougou Formation in Beijing area. These radiometric age constraints for the Changcheng Group (shown in Fig. 1B), including the new SHRIMP zircon age of 1638 ± 14 Ma for the diabase in the Chuanlinggou Formation reported by Gao et al. (2009), suggest that the Chuanlinggou Formation was most likely deposited around $\sim$1.65 Ga—and thus well after the cessation of large-scale IF deposition at $\sim$1.85 Ga.

3. SAMPLES AND METHODS

A total of 55 sedimentary rock samples were analyzed in this study. For 27 out of the 55 samples, iron speciation data were reported previously by Planavsky et al. (2011) as part of a sample compilation but without the detailed geological and geochemical context that we provide here. All outcrop samples were collected in August 2009. Large blocks (>200 g) of the freshest exposures were targeted for sampling, and any surfaces that might have been weathered were trimmed prior to powdering. During rock powdering, we did not observe obvious visible pyrite nodules or bands in our samples, nor were the samples significantly rust stained. Details for the analytical methods are similar to those reported previously in Li et al. (2010, 2012). A concise summary of the Fe, Mo, and S geochemical methods follows.

Concentrations of total Fe (Fe_T) and Mo were measured using an Agilent 7500 quadrupole inductively coupled plasma mass spectrometer (ICP-MS) following a standard multi-acid digestion (HNO_3–HCl–HF). Replicate analyses of USGS standard (SDO-1, $n = 7$) were reproducible within 1.4% and 10.4% for assays of Fe and Mo, respectively. The Fe contents in Fe-carbonates (Fe_{carb}), ferric oxides (Fe_{ox}), and magnetite (Fe_{mag}) were determined using the sequential extraction procedure described in Poulton and Canfield (2005) with quantification by ICP-MS. Disseminated pyrite in samples was extracted using the chromium reduction method described in Canfield et al. (1986) with silver nitrate traps. Resulting Ag_2S precipitates were carefully collected and weighed for the stoichiometric calculation of pyrite sulfur concentration and, in turn, the Fe content present as pyrite (Fe_{py}) in the samples. The quality of Fe_{py} data determined by weighing Ag_2S precipitates was tested by titration of ZnS collected in zinc acetate traps using the same chromium reduction method for five random samples with an average agreement of 5.2%. A subset of samples (10) were tested for the presence of pyrrhotite—given the possibility of pyrite-to-pyrrhotite conversion at the metamorphic grade of the samples—using a HCl and $SnCl_2$ boiling extraction (see details in Planavsky et al., 2011, and Asael et al., 2013). These tests confirmed that pyrrhotite was a minor component of the sulfide pool (<10% of the total sulfide pool).

Carbonate-associated sulfate (CAS) in our samples was extracted using the HCl–$BaCl_2$ procedure similar to that described in Wotte et al. (2012). A brief protocol is given below: (1) 60–130 g of sample powder (200 mesh) were first rinsed with a 10% NaCl solution to remove later stage

sulfate until no dissolved sulfate was observed to precipitate on addition of saturated $BaCl_2$ solution ($\sim$250 g/L) in decanted supernatants. This step typically involved 2–3 rinses. (2) The samples were further rinsed with bleach to remove organic matter, any potential organically bound sulfur, and metastable pyrites until no sulfate was recovered as $BaSO_4$. (3) The samples were then treated with 4 N HCl, which was added in small aliquots to minimize the likelihood that pH fell below 3.8. If a sample contained significant pyrite, which might have oxidized to some degree, 15% $SnCl_2$ was added to the HCl to inhibit possible ferric iron-mediated pyrite oxidation during CAS extraction (Planavsky et al., 2012). (4) Samples were processed by vacuum filtration immediately following the HCl dissolution step to remove the CAS-bearing solution from the insoluble residue within 2 h to minimize further the potential for pyrite oxidation following dissolution. (5) Finally, liberated CAS was precipitated as $BaSO_4$ for subsequent isotopic measurements by adding a saturated $BaCl_2$ solution.

Resulting $BaSO_4$ precipitates, as well as the Ag_2S precipitates resulting from the pyrite extractions, were combusted with an excess of V_2O_5 on a Thermo Scientific Delta V Plus isotope ratio mass spectrometer coupled with a Costech elemental analyzer for determining sulfur isotope compositions of both pyrite ($\delta^{34}S_{py}$) and CAS ($\delta^{34}S_{CAS}$). Sulfur isotope compositions are expressed in standard δ-notation as permil (‰) deviation from the V-CDT international standard with an analytical error of 0.1‰ (1σ) calculated from replicate analyses of IAEA international standards (IAEA-S1, IAEA-S2, IAEA-S3 for $\delta^{34}S_{py}$ and NBS-127, IAEA-SO-5, IAEA-SO-6 for $\delta^{34}S_{CAS}$).

4. RESULTS AND DISCUSSION

4.1. Fe–C systematics

To investigate the marine redox chemistry of the $\sim$1.65 Ga Chuanlinggou Formation, we examined the concentrations of total Fe (Fe_T) as well as extractable Fe grouped operationally by specific mineral types: Fe_{carb}, Fe_{ox}, Fe_{mag}, Fe_{py}, and remaining 'unreactive' Fe (Fe_U) mainly in clay minerals and other silicates. Unlike Fe_U, Fe in the other four mineral groups is reactive enough to form pyrite given sufficient exposure to H_2S either in the water column or during early sediment diagenesis and thus is defined as highly reactive iron (Fe_{HR}). Studies of modern sediments deposited beneath anoxic bottom waters show that Fe_{HR}/Fe_T usually exceeds 0.38 in these settings through inputs of additional Fe_{HR} tied to Fe cycling in the oxygen-deficient water column (Raiswell and Canfield, 1998; Raiswell et al., 2001; Poulton and Raiswell, 2002; reviewed in Lyons and Severmann, 2006, and Poulton and Canfield, 2011). This threshold value has been applied with success in numerous geochemical studies of ancient fine-grained siliciclastic rocks, although thermal alteration can potentially convert Fe_{HR} to Fe_U during burial and reduce this threshold value (Raiswell et al., 2008).

Because the total Fe content remains constant despite any internal redistribution, Fe_T/Al is another way to look for anoxic sedimentary Fe enrichments in rocks that might have experienced burial/metamorphic alteration. Under anoxic bottom waters, modern analogues show that Fe_T/Al usually exceeds $\sim$0.5, nominally the ratio of average continental crust and of most modern and ancient marine muds and shales deposited in oxic environments (Lyons and Severmann, 2006). Sediments deposited beneath oxygen-containing waters but immediately proximal to large anoxic portions of the water column can also have enrichments in highly reactive iron (e.g., Scholz et al., 2014), although such settings are unlikely to leave a spatially and stratigraphically persistent record. Under anoxic and sulfidic (euxinic) bottom waters, Fe_{Py}/Fe_{HR} exceeds 0.7 and often 0.8 because the reactive Fe phases are titrated out of the system before appreciable H_2S starts to accumulate in the water column (Raiswell and Canfield, 1998; Poulton and Canfield, 2011).

Stratigraphic analysis of iron speciation data for the Chuanlinggou Formation reveals two intervals with distinct features (see Fig. 3). The first, a lower interval (LI), comprising subsections CLG2, CLG4, and the lower $\sim$20 m of CLG5, is characterized by low Fe_{HR}/Fe_T [0.19 $\pm$ 0.08 (SD)] and modestly elevated Fe_T/Al ratios (0.67 $\pm$ 0.40), relative to typical continental margin sediments (Lyons and Severmann, 2006). This interval also shows moderate Fe_{Py}/Fe_{HR} ratios (0.31 $\pm$ 0.18). This combination of parameters could be consistent with either ferruginous or oxic bottom-water conditions for the deposition during the LI. The second distinct interval, an upper interval (UI) consisting of the upper part of CLG5 and CLG1, is characterized by higher Fe_{HR}/Fe_T ratios (0.68 $\pm$ 0.12) and higher Fe_T/Al (1.27 $\pm$ 1.05) but lower Fe_{Py}/Fe_{HR} (0.10 $\pm$ 0.12) and similar Fe_T contents (see Fig. 3 and the Appendix), consistent with anoxic and ferruginous conditions for the deposition of the UI. Because of elevated carbonate contents (>50%), some UI samples are not well suited to the Fe-based paleoredox proxies, which were developed for and traditionally applied to fine-grained siliciclastics. However, a recent study based on a large compilation suggests that the Fe_{HR}/Fe_T threshold value of 0.38 can also be valid for carbonate-rich rocks, provided that $Fe_T > 0.5$ wt% (Clarkson et al., 2014), a threshold surpassed by all of the samples examined here.

The UI contains the deepest water facies examined, indicating an increase in the amount of reactive Fe and in the Fe_{HR}/Fe_T ratios that correlate generally with the depth at which the sediments were deposited in the Yanshan Basin. This shift could be linked to the presence of a chemocline—i.e., a switch from oxic to ferruginous conditions with greater depth. There is also a slight increase in average TOC content during the transition to the UI—from 0.67 wt% in LI to 1.16 wt% (Fig. 3 and Appendix). The extent of organic matter loading is often invoked as a proximate driver for anoxic or euxinic water column chemistry below the mixed layer in Proterozoic oceans (e.g., Johnston et al., 2010). However, the lack of iron enrichments in the LI, rather than reflecting deposition beneath oxic waters, could be explained by deposition under anoxic but rapidly accumulating conditions, which can mask the signatures of anoxia via clastic dilution (see Lyons and Severmann, 2006). This might be the case for the LI given
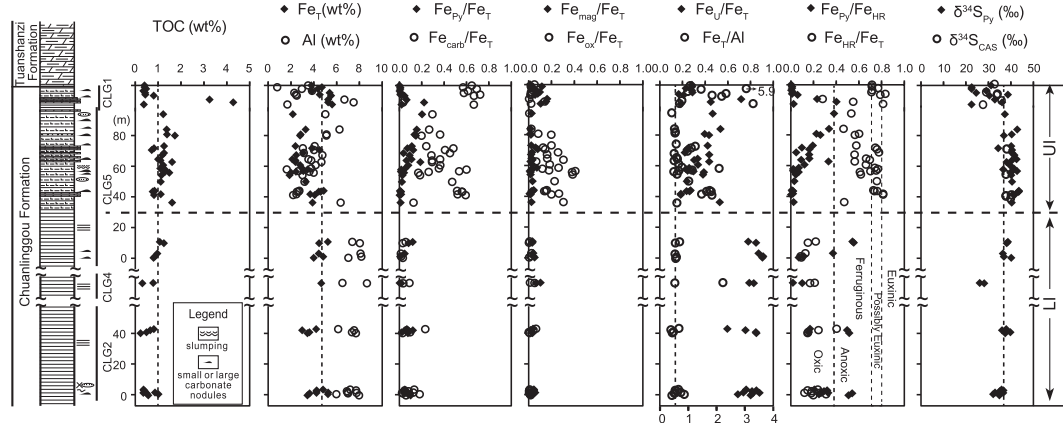
Fig. 3. Composite chemostratigraphy of the Jixian section with new iron speciation data from this study as well as data reported by Planavsky et al. (2011) and related geochemical proxies that provide information for water column redox conditions. UI: upper interval; LI: lower interval. Specific classes of chemically distinguishable iron mineral species are plotted relative to Fe_T in order to show their relative variations from the LI into the UI. From left to right, the dashed lines in boxes represent average of TOC in this study, total Fe of average shales (Turekian and Wedepohl, 1961), average crustal value of Fe_T/Al, boundary values (0.38 for Fe_{HR}/Fe_T and 0.7–0.8 for Fe_{Py}/Fe_{HR}) which differentiate euxinic, ferruginous and oxic waters (see more details in text) and average of S-isotope compositions of pyrites from this study.

the presence of rippled surfaces (in CLG2, see Figs. 1 and 3) suggesting nearshore deposition at potentially high rates of sedimentation.

Strong positive correlation was observed between Fe_{HR}/Fe_T ratios and TIC contents in all samples ($R^2 = 0.9$; Fig. 4A). Furthermore, similar correlations were also observed between Fe_{carb}/Fe_T and TIC for both LI (linear $R^2 = 0.89$) and UI (exponential $R^2 = 0.77$) samples (Fig. 4B), consistent with appreciable ferrous carbonate (e.g., siderite) formation supported by an excess of Fe^{2+}. These correlations are linked to varying amounts of detrital sediments versus authigenic (early diagenetic) carbonate phases.

Despite some ambiguity in the Fe speciation data, there is clearly no evidence for euxinic conditions in subsurface waters for the deepest portion of the Yanshan basin at Jixian. We also note that the internal consistency of our Fe speciation data as demonstrated above (e.g., elevated Fe_{carb} with higher TIC; near zero Fe_{ox}, and

Fe_{mag} in the most-easily-weathered LI black shales) indicate that recent surface weathering is not an issue for these iron ratios and specifically that the pyrite concentrations that can be indicative of euxinia were not lost through later oxidation.

Based on Fe data it seems that non-euxinic conditions were sustained in the subsurface water column of the ~1.65 Ga semi-restricted Yanshan basin. In an anoxic marine system, the development of euxinic versus ferruginous conditions will ultimately be controlled by the flux ratio of Fe^{2+}/SO_4^{2-} into the system, with a proximate control exerted by the need for sufficient organic matter flux to fuel microbial H_2S formation. We did not see an appreciable correlation between pyrite formation (expressed as Fe_{py}/Fe_{HR}) and TOC contents for either our UI samples or all our Chuanlinggou samples ($R^2 = 0.02$; Fig. 5), but this does not necessarily delineate whether sulfate levels or organic matter fluxes were limiting sulfide production and the development of euxinia (more on this below).
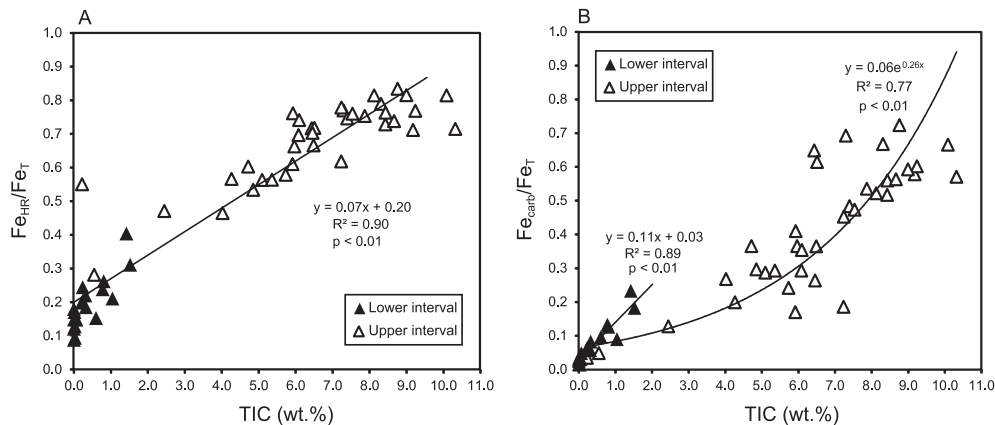

Fig. 4. Crossplots of (A) Fe_{HR}/Fe_T and Fe_{carb}/Fe_T (B), respectively, versus total inorganic carbon (TIC) content in samples from the Chuanlinggou Formation at the Jixian section.
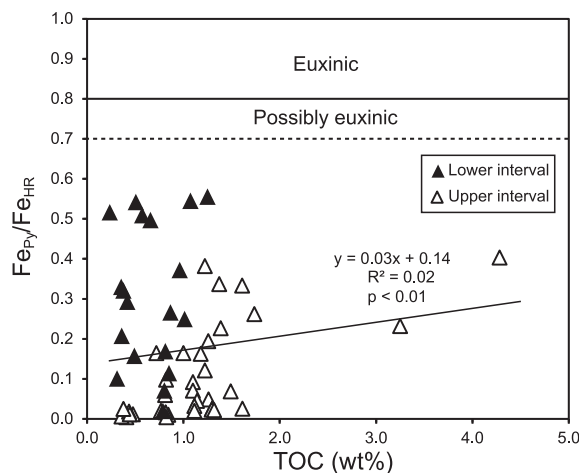
Fig. 5. Crossplot of Fe_{Py}/Fe_{HR} versus total organic carbon (TOC) content in samples from the Chuanlinggou Formation at the Jixian section.

Fig. 6. Frequency distribution of sulfur isotopic composition of pyrite ($\delta^{34}S_{py}$) preserved in the ∼1.65 Ga Chuanlinggou Formation. For comparisons, the isotopic ranges of possible coeval seawater sulfate are shown above the histogram of $\delta^{34}S_{py}$ data. (1): the isotopic composition of carbonate-associate sulfate ($\delta^{34}S_{CAS}$) extracted from the Chuanlinggou Formation (Chu et al., 2007; this study); (2): $\delta^{34}S_{CAS}$ data from ∼1.65 Ga Paradise Creek Formation (Kah et al., 2004; Gellatly and Lyons, 2005); (3): the isotopic composition of coeval seawater sulfate ($\delta^{34}S_{sw}$) suggested by Strauss (1993) based on sulfate evaporite records; (4) a $\delta^{34}S_{sw}$ value of 21‰ suggested by Canfield and Farquhar (2009).

4.2. Sulfur isotopes

In order to explore the sulfur biogeochemistry in the Yanshan basin and further inform the chemistry of late Paleoproterozoic oceans more broadly, we analyzed the isotopic compositions of disseminated pyrites ($\delta^{34}S_{Py}$) and putative coexisting sulfate captured and preserved in the lattice of carbonate minerals (CAS and thus $\delta^{34}S_{CAS}$) of the same sample. Past work reveals that CAS can capture and preserve the isotopic composition of dissolved seawater sulfate (e.g., Burdett et al., 1989; Kah et al., 2004; Gill et al., 2007, 2008; Planavsky et al., 2012). In our case, however, use of the technique is atypical in that we are looking at CAS most likely in diagenetic carbonates (see also Loyd et al., 2012). Therefore, the $\delta^{34}S_{CAS}$ value is expected to capture a pore fluid signal rather than the overlying seawater value. An important implication is that our CAS data are likely to be isotopically heavier than the coeval seawater given the preference for the light isotope, ^{32}S, during bacterial sulfate reduction (BSR). Indeed, the $\delta^{34}S_{CAS}$ values of the Chuanlinggou Formation, which are only available for the carbonate-rich UI samples in this study, range from 27.3‰ to 40.2‰. These values are significantly heavier than the estimated $\delta^{34}S$ of coeval seawater sulfate ($\delta^{34}S_{sw}$) of 21‰ (e.g., Strauss, 1993; Canfield and Farquhar, 2009) and comparable or heavier than previously reported $\delta^{34}S_{CAS}$ values for the Chuanlinggou Formation (Chu et al. (2007) and the ∼1.65 Ga Paradise Creek Formation in Australia (Kah et al., 2004; Gellatly and Lyons, 2005; Fig. 6).

In samples with $\delta^{34}S_{CAS}$ and $\delta^{34}S_{Py}$ values, their difference ($\Delta^{34}S = \delta^{34}S_{CAS} - \delta^{34}S_{Py}$) ranges from −6.8‰ to 4.8‰ (see Appendix; also see Fig. 6). This is a narrow range compared to most modern settings, and the large fractionations often associated with BSR, and could reflect spurious CAS records via pyrite oxidation. However, a few lines of evidence suggest otherwise. First, as described above, we were careful to avoid pyrite oxidation during extraction by using a protocol that minimizes ferric iron-mediated
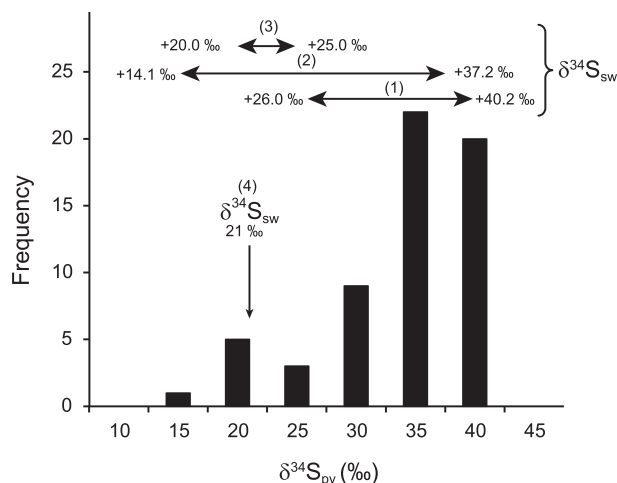
reactions. We also rinsed our samples very carefully to remove any secondary sulfate that might have resulted from outcrop oxidation. Consistent with this level of care, some samples, despite the large amount of material used (>50 g) and their relatively high pyrite contents (see Appendix), failed to yield measurable amounts of CAS. Although CAS is low in our samples, we are confident that our CAS extraction method effectively prevented significant contamination from pyrite oxidation and other non-CAS during the CAS extraction. Also, 83% of our CAS-yielding samples had less than 0.3% Fe_{py} (see Appendix), and many of them contained only trace amounts of pyrite (Fe_{py} < 0.1%), which would limit the potential impact of oxidation during extraction. These samples still show the small $\Delta^{34}S$ range noted above. Most importantly, if pyrite oxidation affected the $\delta^{34}S_{CAS}$ significantly, during extraction or through outcrop weathering, we should see a compressed $\Delta^{34}S$ range—but not negative $\Delta^{34}S$ values given the negligible isotope fractionation during pyrite oxidation (Taylor et al., 1984; Balci et al., 2007).

Peng et al. (2014) suggested that extracted sulfate could be contaminated by recent, secondary atmospherically derived sulfate (SAS). However, we used great care in rinsing our samples, and our $\delta^{34}S_{CAS}$ data are characteristically heavy and thus inconsistent with the much lighter putative SAS contaminants from multiple locations suggested by Peng et al. (2014).

If the small-to-negative $\Delta^{34}S$ values are genuine, as we assert, our observations are significant because they imply the presence of sulfate in pore fluids and sedimentary sulfate reduction under diagenetic conditions. This relationship in

turn indicates that the ferruginous, rather than euxinic, water column implied for the UI was probably not a consequence of sulfate being insufficiently abundant in the water column to fuel BSR in excess of reactive Fe availability.

Given all these considerations, and assuming that the carbonate is diagenetic, pyrite isotopically heavier than coexisting sulfate is most easily explained, at least in our case, by formation that was delayed, from an evolved pore fluid sulfate reservoir—with BSR driving the porewaters isotopically heavier (see also Loyd et al., 2012). Also implicit is earlier capture of the CAS in diagenetic carbonates. Specifically, we tentatively link these negative $\Delta^{34}S$ values to calcium carbonate precipitation in the upper portion of the sediment pile and delayed pyrite formation via sulfidation of Fe carbonates deeper within the sediments. Details of this conceptual model remain unresolved, including the required loss of earlier formed hydrogen sulfide via upward diffusion or some process other than pyrite formation, such as reaction with organic matter. This model, however, is not unreasonable given the expected slower reaction kinetics for iron-rich carbonates compared to labile Fe(III) oxyhydroxide phases, which in this case may have yielded their Fe first, via bacterial reduction, to secondary iron carbonates.

4.3. Mo enrichments

There is iron speciation evidence for ferruginous conditions in the deep-water facies of the Chuanlinggou Formation. In some of the Chuanlinggou samples we investigated, the Fe proxy data yield ambiguous conclusions about depositional redox conditions, but there is no clear evidence for extended periods of euxinia in the late Paleoproterozoic Yanshan Basin—at least in the deepest Jixian area. Reaction with free hydrogen sulfide is a critical player in Mo sedimentary enrichment under anoxic conditions; sulfide is required for the formation of particle reactive thiomolybdates or a Fe–Mo–S phase (e.g., Helz et al., 1996, 2011; Scott and Lyons, 2012). The bulk-rock Mo concentrations

Table 1
Explanation and values for terms used in pore fluid dissolved inorganic carbon model in this study.

Variable	Explanation
ω	Sedimentation rate (cm/yr)
G_0	Utilizable organic carbon (moles $\times$ cm^{-3})
D_s	Sediment diffusion coefficient ($1.92E-5$ cm^2 s^{-1} for CO$_2$, see Boudreau, 1996 table 4.3)
k	Reaction rate for anoxic remineralization (Tromp et al., 1995)
C_0	Marine DIC concentration ($2.2E-6$ mol $\times$ cm^{-3} for modern)
z	Depth (cm)
$\delta^{13}C_{org}$	Carbon isotope value of organic carbon (-25‰)
$\delta^{13}C_{sw}$	Carbon isotope value for marine seawater (0‰)

in our Chuanlinggou samples are on average ~1 ppm (Fig. 7A; Table 1), which is indistinguishable from average crustal values (1–2 ppm). This relationship is consistent with our interpretation of dominantly ferruginous (sulfide-limited) rather than euxinic conditions for the deep waters (Scott et al., 2008) and a lack of significant pore-water sulfide accumulation in the upper, Fe-buffered portion of the sediment pile. The lack of Mo enrichment persists over a relatively wide range of TOC values, in contrast to what is observed in typical euxinic shales (Fig. 7B). This relationship provides critical support for the idea that sediments deposited below ferruginous marine settings are not significant Mo sinks. Therefore, this work supports the argument that the size of the marine Mo reservoir can be used to gauge the extent of euxinic conditions specifically—rather than anoxic conditions more generally (see Reinhard et al., 2013).

4.4. Carbon isotope values in diagenetic carbonates

There are relatively few studies on Proterozoic early diagenetic carbonates despite the possibility that pore fluid
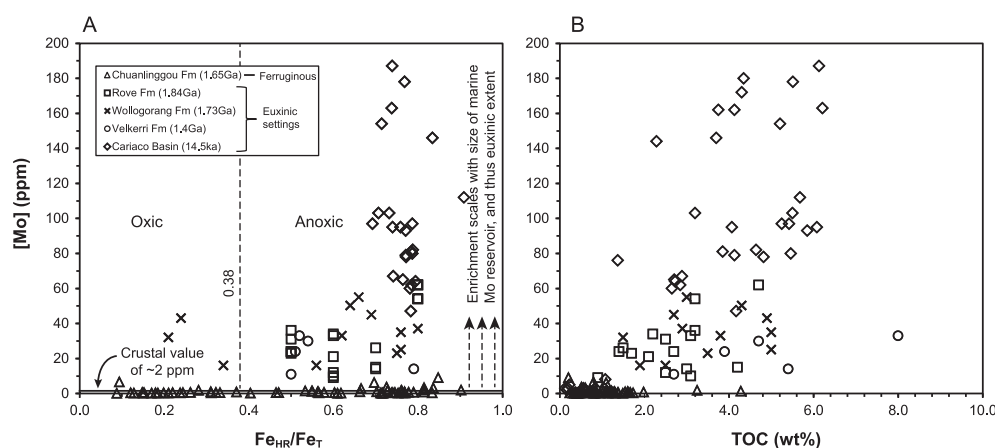
Fig. 7. Compilation of molybdenum concentration versus Fe$_{HR}$/Fe$_T$ (A) and total organic carbon (TOC) (B), respectively for the ferruginous Chuanlinggou Fm. and euxinic Rove Fm. (1.84 Ga), Wollogorang Fm. (1.73 Ga), Velkerri Fm. (1.4 Ga), and modern Cariaco basin (14.5 ka). Data sources: Chuanlinggou Formation (this study), Rove, Wollogorang and Velkerri Formations (Scott et al., 2008), Cariaco basin (Lyons et al., 2003).

carbonate precipitation may have been an important part of the global carbon cycle and global carbon isotope mass balance during the Precambrian. Specifically, it was recently proposed that there was much more extensive precipitation of isotopically light diagenetic carbonates in the Precambrian, when the oceans were more pervasively reducing (Higgins et al., 2009; Johnston et al., 2013; Macdonald et al., 2013; Schrag et al., 2013). This phenomenon could dramatically change estimates of organic carbon burial derived from the marine dissolved inorganic carbon (DIC) record (Schrag et al., 2013). Although the focus of this study is not strictly on diagenetic carbonate formation, our samples provide an excellent opportunity to explore their potential impact on C isotope records. We provide additional discussion on the mode and significance of the diagenetic carbonates of the Chuanlinggou Formation and explore the possible links between marine oxidant levels, ferruginous pore fluids, and the authigenic carbonate sink.

The fact that the examined anoxic calcareous shales of the UI contain extensive diagenetic carbonates (Fig. 2) is consistent with the idea that anoxic remineralization pathways will drive extensive carbonate precipitation (Higgins et al., 2009; Schrag et al., 2013). All of the carbonates from this study have negative $\delta^{13}C$ values, which is consistent with at least partial pore fluid carbonate formation (e.g., Loyd et al., 2012). However, the average $\delta^{13}C$ value ($-3.4 \pm 1.4\permil$) is heavier and less variable than typical marine diagenetic carbonates formed within the zones of sulfate and iron reduction or through anaerobic oxidation of biogenic methane in Phanerozoic sediments (usually between $-6\permil$ and $-60\permil$; e.g., Zhu et al., 2002; Meister et al., 2007; Naehr et al., 2007; Loyd et al., 2012). Given the limited number of samples in this study, additional work will be needed to gauge if this is a common feature of Proterozoic diagenetic carbonates. However, if the Chuanlinggou Formation samples are roughly representative of the isotope values of typical mid-Proterozoic diagenetic carbonates, the data would imply that even extensive authigenic carbonate precipitation is unlikely to significantly alter our traditional view of the global isotope mass balance during this period. Heavier $\delta^{13}C$ values in the Proterozoic relative to comparable Phanerozoic environments could, in theory, be linked to a decrease in the size of the marine DIC reservoir through time—resulting in less effective isotopic buffering of pore fluid DIC in younger sediments (Bartley and Kah, 2004). Alternatively, limited pore fluid oxidants—lower sulfate concentrations and (or) a limiting ferric iron supply (with non-bioturbated sediments supporting little to no continuous Fe re-oxidation)—may have led to more extensive precipitation of carbonates in the methanic zone, which is typically characterized by positive $\delta^{13}C_{DIC}$ values (see Naehr et al., 2007, and references therein). We explore this possibility below.

A simple early diagenetic model (Berner, 1964, 1971) can be used to gauge the factors controlling the $\delta^{13}C$ of diagenetic carbonates precipitated in anoxic pore fluids. With this approach it is straightforward to illustrate and roughly quantify the main processes that will control the pore fluid

DIC carbon isotope values, allowing exploration of the potential influence of oxidant limitation and methanogenesis on the $\delta^{13}C$ of the diagenetic carbonates of the Chuanlinggou Formation.

We calculate pore fluid [DIC] using a modified version of the one-dimensional general diagenetic equation for the chemical evolution of a fluid phase within the sediment (G-model; Berner, 1964):

$$\frac{\partial C}{\partial t} = D_s \frac{\partial^2 C}{\partial z^2} - \omega \frac{\partial C}{\partial z} + kG_0 \exp\left[-\frac{k}{\omega}z\right] \qquad (1)$$

where the terms on the right hand side denote mass conservation due to fluxes associated with diffusion (term 1), advection (term 2), and reaction (term 3). These fluxes are, in turn, controlled by the sediment diffusion coefficient a given species (D_s), the concentration gradient as a function of depth in the sediment [$\partial C/\partial z$, where z is depth (positive downward)], the sediment advection velocity (ω), and a first-order reaction term for the conversion of labile organic matter to DIC. In the latter term, k represents the intrinsic rate of organic carbon remineralization, and G_0 represents the concentration of metabolically available organic carbon at the sediment–water interface. For simplicity, we assume a scaling between k and ω generalized to anoxic mineralization during sulfate reduction (e.g., Tromp et al., 1995). Assuming steady state ($\partial C/\partial t = 0$) and the boundary condition $C(z = \infty) = C_\infty$, we obtain the analytical solution:

$$C(z) = -\frac{\omega^2 G_0}{D_s k + \omega^2} \exp\left[-\frac{k}{\omega}z\right] + C_\infty \qquad (2)$$

If we further specify the boundary condition that the DIC concentration at the sediment–water interface is equal to that of the overlying seawater [$C(z = 0) = C_0 = [DIC]_{SW}$], we can obtain a solution for C_∞, and this can be combined with Eq. (2) above to obtain a solution for [DIC]$_{total}$ as a function of depth in the sediment:

$$C(z) = -\frac{\omega^2 G_0}{D_s k + \omega^2} \exp\left[-\frac{k}{\omega}z\right] + \frac{\omega^2 G_0}{D_s k + \omega^2} + C_0 \qquad (3)$$

We can then take the difference between [DIC]$_{total}$ and [DIC]$_{SW}$ to determine [DIC]$_{remin}$, and through simple mass balance determine the carbon isotope composition of the pore fluid DIC:

$$[DIC]_{total}\delta^{13}C_{total} = [DIC]_{remin}\delta^{13}C_{remin} + [DIC]_{SW}\delta^{13}C_{SW} \qquad (4)$$

All values/ranges for model parameters are listed in Table 1.

The model results are given in Fig. 8. Three significant points emerge from this basic analysis. First, availability of initial utilizable organic carbon (i.e., G_0) has a significant impact on pore fluid $\delta^{13}C_{DIC}$ values (Fig. 8A). Although it is difficult to constrain values for G_0, even in modern systems, bulk TOC values in the Chuanlinggou sediments hosting the diagenetic beds (upper Subsection CLG5) are near 1% (Fig. 3, Appendix). We thus consider a reasonable minimum estimate to be >1% for initial utilizable organic carbon for the Chuanlinggou diagenetic carbonates.
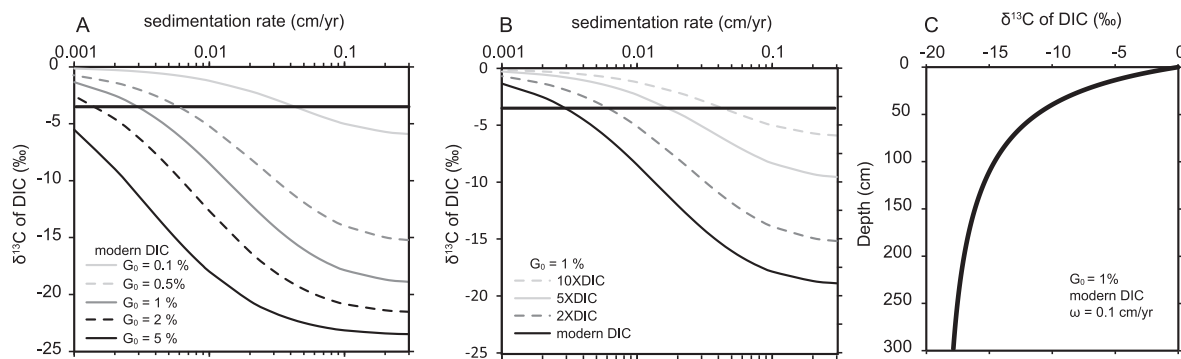
Fig. 8. Modeling for $\delta^{13}C$ of dissolved inorganic carbon (DIC) in pore fluids. (A) Sensitivity analyses for $\delta^{13}C$ of DIC versus sedimentation rate with contours representing utilizable organic carbon (G_0). (B) Sensitivity analyses for $\delta^{13}C$ of DIC versus sedimentation rate with contours representing marine DIC concentrations. G_0 is equal to 1%. (C) $\delta^{13}C$ of DIC with G_0 of 1%, modern marine DIC concentrations, and ω of 0.1 cm/yr. For all contour plots, results are taken from 3 m depth, assuming oxidants will be exhausted below this depth. The horizontal black lines in (A) and (B) represent the average $\delta^{13}C$ of the diagenetic carbonates of the Chuanlinggou Formation. See text for detailed description of model setup.

Second, it is clear from Fig. 8A,B that sedimentation rates also have the capacity to cause large variations in the $\delta^{13}C$ of pore fluid DIC. However, with reasonable sedimentation rates for the examined settings over short time scales (e.g., ~0.1 cm/yr on sub-million year timescales; Sadler, 1981), and with modern [DIC] and G_0 of 1%, it becomes difficult to explain the average $\delta^{13}C$ of the diagenetic carbonates if carbonate precipitation happened only in the sulfate and iron reduction diagenetic zones (Fig. 8C). The data would thus seem to imply a non-trivial portion of diagenetic carbonate formation in the deeper methanic zone of the sediment column.

Third, changes in seawater [DIC] result in significant shifts in pore fluid $\delta^{13}C_{DIC}$ values (Fig. 8B and A). With very high marine DIC concentrations, there is significant isotopic buffering capacity, making it increasingly difficult to drive pore fluid DIC to lighter $\delta^{13}C$ values. However, reasonable estimates of sedimentation rate (e.g., between 0.05 and 0.1 cm/yr) and inputs of organic carbon (for the examined sections) yield pore fluid $\delta^{13}C_{DIC}$ values significantly lighter than the $\delta^{13}C$ of the examined diagenetic carbonates (Fig. 8A); this prediction is true even with very elevated DIC concentrations (>5× modern [DIC]; Fig. 8B). This leaves us with the intriguing possibility that carbonate formation in the methanic zone, likely linked to pore fluid oxidant limitation (see more below), was an important factor behind the relatively heavy $\delta^{13}C$ of the diagenetic carbonates. Consistent with this model, diagenetic carbonates from the extremely organic-rich Jurassic Kimmeridge Clay have average $\delta^{13}C$ values near $-3‰$ because of carbonate precipitation in the methanic zone (Irwin et al., 1977).

Significant carbonate precipitation in the methanic zone in the Proterozoic may be linked with low marine oxidant (primarily sulfate) concentrations and less net sulfate reduction compared to 'typical' modern continental margin sediments. In other words, if seawater sulfate concentrations were a small fraction of modern levels during the mid-Proterozoic and quickly consumed in the sediments, a relatively

thin zone of sulfate reduction may have caused limited evolution of $\delta^{13}C$ of DIC. Within the zone of methanogenesis, following sulfate consumption, the $\delta^{13}C$ of DIC would be expected to shift to heavier values, as isotopically light carbon is preferentially utilized for methane formation from the existing DIC pool. In this case, the result is relatively ^{13}C-enriched authigenic carbonate phases due fundamentally to oxidant limitation in Proterozoic seawater. Of course, oxygen would have been absent beneath the anoxic bottom waters, and a number of studies point to low sulfate in the ocean (e.g., Kah et al., 2004; Scott et al., 2014) and low atmospheric O_2 at this time (e.g., Planavsky et al., 2014). We propose that porewater oxidant limitation is likely to have prevented authigenic carbonates from being a major sink—in terms of the global mass balance—for isotopically light carbon.

There is currently a lack of strong empirical evidence for widespread isotopically light carbonate burial in marginal marine environments during the Proterozoic, but if authigenic carbonates were buried primarily in deep water environments one might expect this record to be poorly preserved (e.g., Canfield and Kump, 2013). Given that decreasing the sedimentation rate and initial utilizable organic carbon concentrations results in heavier pore fluid $\delta^{13}C_{DIC}$ values, it may be difficult for distal marine environments to support significant burial fluxes of authigenic carbonate with markedly light $\delta^{13}C$ values. Given this framework, the search for evidence of a significant isotopically light carbon sink in the Proterozoic should focus on well-preserved continental shelf settings. However, carbonate precipitation in the methanic zone may be less important in offshore than marginal settings due to lower relative organic carbon loading. If this is the case the result that offshore marine settings (compared to more organic-rich settings) may be more suited for burial of isolated depleted carbonate despite heavier porewater DIC values in the sulfate reduction zone of the sediment column. It could be possible to resolve between these competing

models with a more complex, spatially resolved coupled early diagenetic and ocean modeling approach.

4.5. Broader implications for the middle Proterozoic ocean chemistry

Ocean chemistry and redox structure in the late Paleoproterozoic (1.8–1.6 Ga) is particularly intriguing because it is believed to mark a fundamental transition of ocean redox state after which major iron formations (IF) largely disappeared from the rock record for a billion years. As stated in Section 1, transitions from ferruginous to mildly oxic-suboxic (Holland, 2006; Slack et al., 2007, 2009) or euxinic (Canfield, 1998) deep ocean waters were the two major mechanisms proposed previously to explain the global termination of large IF deposition. In particular, the euxinia hypothesis received support from sedimentary Fe speciation, S isotope systematics, and lipid biomarker data collected from mid-Proterozoic marine basins (e.g., Brocks et al., 2005; Poulton et al., 2004; Shen et al., 2002, 2003). In contrast, new Fe speciation data for the <1.84 Ga Rove Formation (Animikie Group, Lake Superior region) suggest mid-depth euxinic waters associated with deeper ferruginous waters (Poulton et al., 2010), which is an emerging idea for the Precambrian ocean more generally, including the late Archean (Reinhard et al., 2009; Scott et al., 2011) and Neoproterozoic (Canfield et al., 2008; Li et al., 2010, 2012; Johnston et al., 2010; see Lyons et al., 2014, for review). Our Fe–S–C–Mo data from the Chuanlinggou Formation indicate non-euxinic (i.e., ferruginous and possibly oxic) subsurface marine conditions for the deepest portion of the ∼1.65 Ga Yanshan basin. We suggest that this condition may have been due to insufficient water column sulfate reduction rates (relative to reactive Fe delivery fluxes). This suggestion is supported by the occurrences of ironstones in the Chuanlinggou Formation in Jiaxian area (Planavsky et al., 2014) and the west part of basin (e.g., Xuanhua area) where economic ironstones were deposited and mined historically. This situation is in contrast to many modern semi-restricted euxinic marine settings (e.g., the Black Sea and Cariaco Basin) where both sulfate and organic matter fluxes are not limiting factors for the development of euxinia. This observation is also in contrast to the Cryogenian interglacial semi-restricted Nanhua Basin (South China) where euxinia developed in the subsurface waters of the basin when the post-Sturtian transgression brought nutrient-rich deep seawater from the open ocean into the basin, resulting in higher productivity in its surface water and, in turn, in high export of organic matter into subsurface water (Li et al., 2012).

We observed, however, that the extent of euxinia seems to be decoupled from local organic matter loading in most mid-Proterozoic settings. A compilation of paired Fe_{py}/Fe_{HR} and TOC data reported for numerous mid-Proterozoic strata shows no significant correlation between relative pyritization and TOC content (Fig. 9A). This also is true when we screened the dataset to only include samples deposited under anoxic conditions (Fig. 9B). The suggestion is that other

factors beyond just local organic matter loading (which are linked to TOC values) control dissolved sulfide-ferrous iron ratios. These controls include broader, *regional* patterns of organic carbon delivery and related rates of BSR relative to pervasive availability of sulfide-buffering dissolved Fe. Other work leaves open the possibility that sulfate could have been a limiting factor in the development of Proterozoic euxinia (Li et al., 2010).
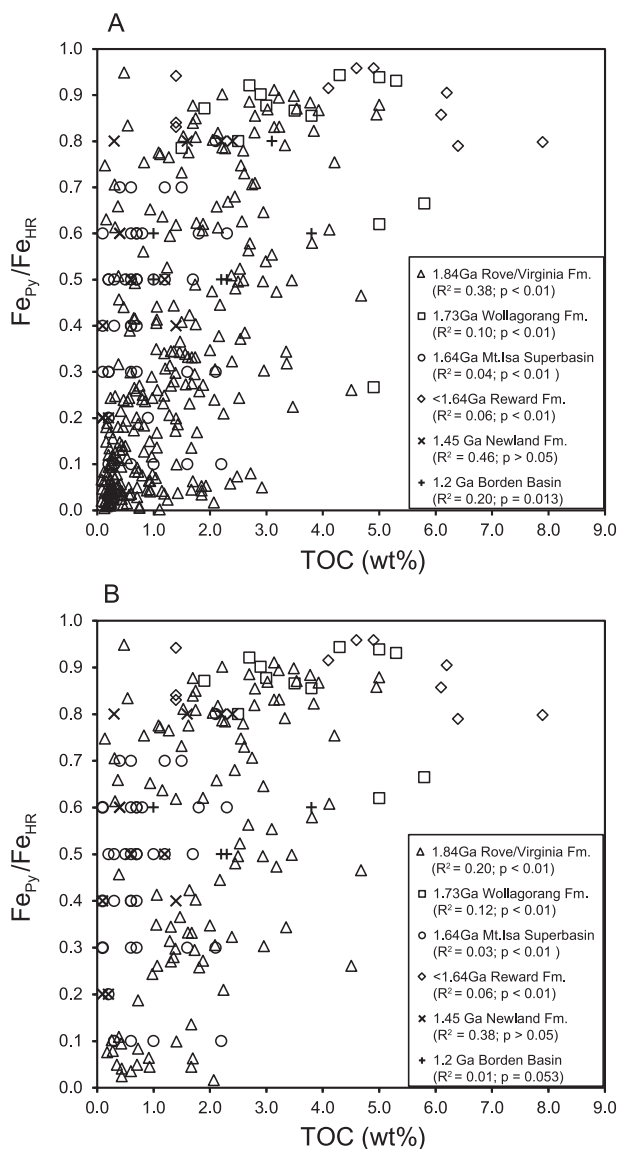
Fig. 9. Compilation of Fe_{Py}/Fe_{HR} versus total organic carbon (TOC) content reported for the mid-Proterozoic strata. (A) Dataset includes both oxic and anoxic samples. (B) Dataset includes only unambiguous anoxic samples (i.e., $Fe_{HR}/Fe_T > 0.38$). Coefficient (R^2) between Fe_{Py}/Fe_{HR} and TOC and t-test p value for the dataset are given in brackets for each strata unit in legend. Data source: 1.84 Ga Rove/Virginia Fm. (Poulton et al., 2004, 2010), 1.73 Ga Wollogorang and < 1.64 Ga Reward Fms. (Shen et al., 2002), 1.64 Ga Mt. Isa Superbasin, 1.45 Ga Newland Fm. and 1.2 Ga Borden Basin (Planavsky et al., 2011).

5. SUMMARY AND CONCLUSIONS

Our Fe–S–C–Mo biogeochemical investigation of strata from the ~1.65 Ga Chuanlinggou Formation yields results that are consistent with non-euxinic water column conditions (ferruginous and possibly oxic) persisting in the subsurface waters of the semi-restricted Yanshan rift basin—at least in the deepest Jixian area. The non-correlative relationships between relative pyritization (represented by Fe_{py}/Fe_{HR}) and TOC observed for both the Chuanlinggou Formation and other previously studied mid-Proterozoic strata support that other factors beyond just *local* organic matter loading must be considered for euxinic development in mid-Proterozoic oceans. However, paired CAS-pyrite S-isotope data from the Chuanlinggou Formation suggest the persistence of sulfate into the pore fluids, which is not consistent with insufficient sulfate for BSR in water column. In addition, despite evidence for deposition under anoxic conditions, there are not significant Mo enrichments in the Chuanlinggou Formation. This observation supports the idea that the presence of appreciable dissolved sulfide in the water column is a key control in Mo enrichment and that the size of the marine Mo reservoir can be used to gauge the extent of euxinic conditions specifically—rather than anoxic conditions more generally (cf. Reinhard et al., 2013).

Lastly, there appears to have been extensive diagenetic carbonate precipitation during the deposition of the Chuanlinggou Formation, consistent with the idea of enhanced precipitation in anoxic pore fluids during the Precambrian (Schrag et al., 2013). However, these carbonates have only moderately negative $\delta^{13}C$ values ($-3.4 \pm 1.4‰$), which we link, with support from a simple numerical model, to extensive precipitation of carbonates in the methanic zone within the sediments. Oxidant limitation (sulfate in particular) in the pore fluids could have led to more extensive precipitation of carbonates in the methanic zone, which is characterized by positive $\delta^{13}C_{DIC}$ values.

ACKNOWLEDGEMENTS

APPENDIX

Table A
Key geochemical data of the Chuanlinggou Formation at Jixian section.

Sample	Depth[a] (m)	TIC (%)	TOC (%)	Al (%)	Mn (%)	Fe_Py (%)	Fe_carb (%)	Fe_ox (%)	Fe_mag (%)	Fe_HR (%)	Fe_U (%)	Fe_T (%)	Fe_HR/Fe_T	Fe_Py/Fe_HR	Fe_T/Al	δ34S_Py (‰)	δ34S_CAS (‰)	Δ34S (‰)	δ13C_Carb (‰)	δ18O_Carb (‰)	Mo (ppm)	Mo/TOC (ppm/wt%)
Upper Interval (UI)																						
CLGI-13	12.5	6.4	0.4	3.5	0.16	0.01	2.46	0.19	0.05	2.72	1.08	3.80	0.72	0.00	1.08	31.2	32.4	1.2	-3.2	-8.1	0.3	0.7
CLGI-12	11.3	10.3	0.4	0.8	0.33	0.04	2.69	0.09	0.55	3.37	1.35	4.72	0.71	0.01	5.94	22.6					0.2	0.5
CLGI-11	10.2	7.3	0.5	3.0	0.21	0.04	3.01	0.12	0.18	3.35	1.00	4.35	0.77	0.01	1.47	22.5					0.2	0.5
CLGI-10	8.9	6.5	0.4	3.9	0.17	0.02	2.36	0.13	0.25	2.75	1.08	3.84	0.72	0.01	1.00	29.1	32.5	3.4	-3.2	-8.2	0.2	0.6
CLGI-09	7.6	9.2	0.4	2.3	0.27	0.07	3.12	0.12	0.53	3.84	1.56	5.40	0.71	0.02	2.36	24.6	28.7	4.1	-3.1	-8.0	0.3	0.6
CLGI-08	6.5	8.8	0.8	2.4	0.23	0.04	3.28	0.10	0.36	3.78	0.75	4.53	0.83	0.01	1.86	38.7	33.7	-5.0	-3.2	-8.3	0.3	0.7
CLGI-07	5.8	8.3	0.8	2.5	0.24	0.26	3.68	0.10	0.32	4.36	1.16	5.52	0.79	0.06	2.20	30.5	33.4	2.9	-3.6	-8.7	0.7	0.9
CLGI-03	3.2	0.5	3.2	6.7	0.08	0.34	0.26	0.03	0.85	1.48	3.79	5.27	0.28	0.23	0.79	32.9					1.9	0.6
CLGI-02	1.4	0.2	4.3	7.5	0.19	1.17	0.18	0.74	0.80	2.90	2.37	5.26	0.55	0.40	0.70	36.1					1.3	0.3
CLGI-01	0	10.1	0.4	1.7	0.25	0.11	3.74	0.13	0.59	4.57	1.04	5.61	0.81	0.02	3.32	22.5	27.3	4.8	-3.3	-8.5	0.8	2.2
CLG5-53	93.6	4.9	1.2	5.0	0.03	0.44	0.64	0.02	0.06	1.16	1.01	2.17	0.53	0.38	0.43	37.4	35.5	-1.9	-2.4	-12.3	1.5	1.2
CLG5-45	83.6	4.0	1.4	6.3	0.05	0.51	0.88	0.08	0.05	1.53	1.76	3.28	0.46	0.34	0.52	42.9	37.5	-5.4	-2.6	-10.5	0.5	0.3
CLG5-44	80.4	4.7	1.4	5.1	0.04	0.39	1.05	0.24	0.05	1.73	1.14	2.86	0.60	0.23	0.56	40.4			-2.4	-11.5	0.5	0.4
CLG5-43	79.7	4.3	1.7	5.1	0.03	0.41	0.56	0.56	0.06	1.58	1.21	2.79	0.57	0.26	0.55	36.9					0.4	0.2
CLG5-39	72.8	5.7	1.3	4.1	0.03	0.27	0.58	0.48	0.06	1.38	1.01	2.39	0.58	0.19	0.59	40.2	37.2	-3.0	-2.3	-12.5	0.5	0.4
CLG5-38	71.4	7.4	0.8	3.0	0.07	0.28	1.86	0.49	0.24	2.87	0.98	3.84	0.75	0.10	1.26	34.4	38.2	3.8	-2.8	-11.1	0.6	0.7

Sample																						
CLG5-37	70.3	5.9	0.7	4.0	0.07	0.56	1.85	0.66	0.36	3.44	1.08	4.52	0.76	0.16	1.12	40.6	37.8	−2.8	−2.4	−11.8	1.8	2.5
CLG5-36	68.3	7.2	1.3	3.1	0.08	0.12	1.39	0.79	0.09	2.39	0.68	3.07	0.78	0.05	0.98	40.6					0.7	0.6
CLG5-35	66.9	5.1	1.2	4.8	0.04	0.23	0.71	0.40	0.06	1.39	1.08	2.46	0.56	0.16	0.52	41.6					0.7	0.6
CLG5-33	64.3	6.5	1.0	3.5	0.05	0.23	0.77	0.35	0.06	1.41	0.71	2.11	0.67	0.16	0.60	42.6					2.8	2.8
CLG5-32	63.5	6.1	1.1	3.8	0.05	0.15	0.70	0.73	0.08	1.67	0.73	2.39	0.70	0.09	0.63	40.5					6.2	5.7
CLG5-31	62.4	5.4	1.6	4.7	0.05	0.45	0.70	0.16	0.04	1.35	1.05	2.40	0.56	0.33	0.51	38.1			−2.4	−11.8	1.1	0.7
CLG5-29	60.4	6.0	1.2	4.2	0.07	0.23	1.03	0.52	0.09	1.86	0.95	2.81	0.66	0.12	0.67	39.6	37.5	−2.1	−2.5	−10.9	0.9	0.7
CLG5-27	58.3	6.1	1.1	3.8	0.06	0.16	1.05	0.78	0.22	2.21	0.77	2.98	0.74	0.07	0.79	41.4					0.4	0.4
CLG5-25	56.1	6.5	1.3	3.6	0.05	0.05	0.64	1.00	0.03	1.72	0.73	2.44	0.70	0.03	0.68	40.4	37.8	−2.6	−2.5	−11.3	1.0	0.8
CLG5-24	57.6	9.2	1.3	1.6	0.11	0.06	2.08	0.42	0.10	2.66	0.80	3.46	0.77	0.02	2.11	36.6					1.0	0.7
CLG5-23	56.5	7.9	1.3	2.7	0.09	0.05	1.65	0.55	0.07	2.32	0.76	3.08	0.75	0.02	1.16	42.8					0.2	0.2
CLG5-22	55.5	5.9	1.5	4.0	0.03	0.08	0.34	0.77	0.03	1.23	0.78	2.01	0.61	0.07	0.50	39.8			−2.4	−12.3	0.2	0.1
CLG5-21	53.9	7.2	1.1	3.0	0.04	0.05	0.35	0.72	0.03	1.16	0.71	1.87	0.62	0.04	0.62	40.2					0.3	0.2
CLG5-19	49.6	7.5	1.1	3.2	0.09	0.08	1.56	0.75	0.11	2.51	0.79	3.30	0.76	0.03	1.03	40.6					1.3	1.2
CLG5-16	43.7	8.4	0.8	2.7	0.16	0.04	2.52	0.77	0.22	3.55	1.32	4.87	0.73	0.01	1.77	43.6	40.2	−3.4	−6.4	−8.4	1.6	1.9
CLG5-15B	43.2	8.4	0.8	2.7	0.15	0.07	2.49	0.66	0.17	3.39	1.06	4.45	0.76	0.02	1.67	43.6	37.8	−5.8			0.4	0.5
CLG5-15A	43.2	8.7	0.8	2.5	0.16	0.06	2.60	0.63	0.11	3.41	1.21	4.62	0.74	0.02	1.83	43.3	37.8	−5.5	−6.5	−8.3	0.3	0.4
CLG5-13	41.45	8.1	1.1	2.5	0.13	0.06	1.93	0.98	0.04	3.01	0.69	3.69	0.81	0.02	1.49	41.0	39.9	−1.1	−4.9	−8.4	2.0	1.8
CLG5-12	40.9	9.0	0.8	2.2	0.16	0.01	2.42	0.82	0.07	3.33	0.76	4.09	0.81	0.00	1.86	41.6	34.8	−6.8	−5.9	−8.0	3.3	4.1
CLG5-09	36	2.4	1.6	6.4	0.05	0.05	0.50	1.19	0.10	1.84	2.06	3.90	0.47	0.03	0.61	40.4					0.5	0.3
Lower Interval (LI)																						
CLG5-08B	10.4	0.3	1.1	7.4	0.02	0.63	0.30	0.04	0.18	1.15	4.08	5.23	0.22	0.55	0.71	38.7					0.5	0.4
CLG5-08A	9.6	0.1	1.3	8.0	0.01	0.37	0.14	0.01	0.15	0.67	3.80	4.47	0.15	0.56	0.56	38.2					0.2	0.2
CLG5-03	2.8	0.0	1.0	8.1	0.01	0.21	0.06	0.11	0.18	0.57	3.87	4.44	0.13	0.37	0.55	36.5					0.3	0.3
CLG5-02	0.8	0.0	0.9	8.2	0.01	0.05	0.08	0.09	0.21	0.42	4.40	4.83	0.09	0.11	0.59	36.9					0.2	0.2
CLG5-01	0	0.0	0.8	7.0	0.01	0.03	0.12	0.02	0.21	0.38	3.62	3.99	0.09	0.07	0.57	40.2					6.6	8.2
CLG4-05	37.7	1.0	0.8	6.5	0.10	0.06	1.31	0.18	1.52	3.08	11.53	14.61	0.21	0.02	2.24	26.2					0.2	0.3
CLG4-03	37.5	0.0	0.3	8.7	0.02	0.08	0.17	0.25	0.30	0.79	3.87	4.66	0.17	0.10	0.54	28.2					0.2	0.7
CLG2-14	43.2	1.4	0.8	6.1	0.06	0.29	0.98	0.27	0.16	1.70	2.51	4.21	0.40	0.17	0.69	38.0					0.3	0.3
CLG2-12	42.4	0.2	0.7	7.5	0.01	0.36	0.19	0.13	0.05	0.73	2.26	2.99	0.24	0.50	0.40	36.1					0.5	0.8
CLG2-10	41.1	0.6	0.5	7.3	0.03	0.09	0.35	0.01	0.11	0.55	3.06	3.61	0.15	0.16	0.49	39.8					0.4	0.7
CLG2-09	40.5	0.0	0.2	7.7	0.01	0.26	0.10	0.03	0.12	0.51	2.94	3.45	0.15	0.52	0.45	37.5					0.3	1.3
CLG2-08	3.8	0.8	0.4	7.2	0.04	0.24	0.64	0.05	0.22	1.15	3.67	4.81	0.24	0.21	0.67	35.9					0.4	1.0
CLG2-06	3.2	0.1	0.4	7.7	0.01	0.20	0.21	0.03	0.19	0.63	3.62	4.25	0.15	0.32	0.55	36.7					0.5	1.3
CLG2-05	2.7	0.3	0.4	6.9	0.02	0.23	0.35	0.02	0.19	0.78	3.45	4.23	0.19	0.29	0.61	35.1					0.3	0.6
CLG2-04B	1.6	0.0	0.4	7.8	0.01	0.17	0.11	0.09	0.15	0.51	3.72	4.24	0.12	0.33	0.55	36.6					0.4	1.0
CLG2-04A	1.8	0.8	0.9	7.0	0.04	0.37	0.66	0.05	0.30	1.38	3.88	5.26	0.26	0.27	0.75	33.0					0.6	0.7
CLG2-03	1.3	0.0	0.5	7.0	0.00	0.35	0.12	0.02	0.16	0.65	2.98	3.63	0.18	0.54	0.52	34.7					0.3	0.6
CLG2-02	0.7	1.5	1.0	6.0	0.06	0.41	0.96	0.07	0.20	1.63	3.62	5.25	0.31	0.25	0.88	32.2					0.4	0.4
CLG2-01	0	0.2	0.6	8.0	0.02	0.35	0.21	0.06	0.07	0.69	2.77	3.45	0.20	0.51	0.43	34.9					0.3	0.5

[a] Depths are relative to zero at the bottom of each subsection.

REFERENCES

Algeo T. J., Chen Z., Fraiser M. L. and Twitchett R. J. (2011) Terrestrial–marine teleconnections in the collapse and rebuilding of Early Triassic marine ecosystems. *Palaeogeogr. Palaeoclimatol. Palaeoecol.* **308**, 1–11.

Anbar A. D. and Knoll A. H. (2002) Proterozoic ocean chemistry and evolution: a bioinorganic bridge. *Science* **297**, 1137–1142.

Asael D., Tissot F. L. H., Reinhard C. T., Rouxel O., Dauphas N., Lyons T. W., Ponzevera E., Liorzou C. and Cheron S. (2013) Coupled molybdenum, iron and uranium stable isotopes as oceanic paleoredox proxies during the Paleoproterozoic Shunga Event. *Chem. Geol.* **362**, 193–210.

Balci N., Shanks, III, W. C., Mayer B. and Mandernack K. W. (2007) Oxygen and sulfur isotope systematics of sulfate produced by bacterial and abiotic oxidation of pyrite. *Geochim. Cosmochim. Acta* **71**, 3796–3811.

Bartley J. K. and Kah L. C. (2004) Marine carbon reservoir, C_{org}–C_{carb} coupling, and the evolution of the Proterozoic carbon cycle. *Geology* **32**, 129–132.

Bekker A., Slack J. F., Planavsky N., Krapež B., Hofmann A., Konhauser K. O. and Rouxel O. J. (2010) Iron formation: the sedimentary product of a complex interplay among mantle, tectonic, oceanic, and biospheric processes. *Econ. Geol.* **105**, 467–508.

Berner R. A. (1964) An idealized model of dissolved sulfate distribution in recent sediments. *Geochim. Cosmochim. Acta* **28**, 1497–1503.

Berner R. A. (1971) *Principles of Chemical Sedimentology*. McGraw-Hill, New York.

Boudreau B. P. (1996) The diffusive tortuosity of fine-grained unlithified sediments. *Geochim. Cosmochim. Acta* **60**, 3139–3142.

Brocks J. J., Love G. D., Summons R. E., Knoll A. H., Logan G. A. and Bowden S. A. (2005) Biomarker evidence for green and purple sulphur bacteria in a stratified Palaeoproterozoic sea. *Nature* **437**, 866–870.

Burdett J. W., Arthur M. A. and Richardson M. (1989) A Neogene seawater sulfur isotope age curve from calcareous pelagic microfossils. *Earth Planet. Sci. Lett.* **94**, 189–198.

Canfield D. E. (1998) A new model for Proterozoic ocean chemistry. *Nature* **396**, 450–453.

Canfield D. E. and Farquhar J. (2009) Animal evolution, bioturbation, and the sulfate concentration of the oceans. *Proc. Natl. Acad. Sci. USA* **106**, 8123–8127.

Canfield D. E. and Kump L. R. (2013) Carbon cycle makeover. *Science* **339**, 533–534.

Canfield D. E., Raiswell R., Westrich J. T., Reaves C. M. and Berner R. A. (1986) The use of chromium reduction in the analysis of reduced inorganic sulfur in sediments and shales. *Chem. Geol.* **54**, 149–155.

Canfield D. E., Poulton S. W., Knoll A. H., Narbonne G. M., Ross G., Goldberg T. and Strauss H. (2008) Ferruginous conditions dominated later Neoproterozoic deep-water chemistry. *Science* **321**, 949–952.

Chen J. B., Zhang H. M., Zhu S. X., Zhao Z. and Wang Z. G. (1980) Research on Sinian Suberathem of Jixian Tianjin (in Chinese). In *Research on Precambrian Geology: Sinian Suberathem in China* (eds. Tianjin Institute of Geology and Mineral Resources and CAGS). Tianjin Sci. & Tech. Press, Tianjin, pp. 56–114.

Chu X. L., Zhang T. G., Zhang Q. R. and Lyons T. W. (2007) Sulfur and carbon isotope records from 1700 to 800 Ma carbonates of the Jixian section, northern China: implications for secular isotope variations in Proterozoic seawater and relationships to global supercontinental events. *Geochim. Cosmochim. Acta* **71**, 4668–4692.

Clarkson M. O., Poulton S. W., Guilbaud R. and Wood R. A. (2014) Assessing the utility of Fe/Al and Fe-speciation to record water column redox conditions in carbonate-rich sediments. *Chem. Geol.*. http://dx.doi.org/10.1016/j.chemgeo.2014.05.031.

Feng L., Li C., Huang J., Chang H. and Chu X. (2014) A sulfate control on marine mid-depth euxinia on the early Cambrian (ca. 529–521 Ma) Yangtze platform, South China. *Precambrian Res.* **246**, 123–133.

Gao L. Z., Zhang C. H., Yin C. Y., Shi X. Y., Wang Z. Q., Liu Y. M., Liu P. J., Tang F. and Song B. (2008) SHRIMP zircon ages: basis for refining the chronostratigraphic classification of the Meso- and Neoproterozoic strata in North China Old Land. *Acta Geosci. Sin.* **29**, 366–376.

Gao L. Z., Zhang C. H., Liu P. J., Ding X. Z., Wang Z. Q. and Zhang Y. J. (2009) Recognition of Meso- and Neoproterozoic stratigraphic framework in North and South China. *Acta Geosci. Sin.* **30**, 433–446.

Gellatly A. M. and Lyons T. W. (2005) Trace sulfate in mid-Proterozoic carbonates and the sulfur isotope record of biospheric evolution. *Geochim. Cosmochim. Acta* **69**, 3813–3829.

Gill B. C., Lyons T. W. and Saltzman M. R. (2007) Parallel, high-resolution carbon and sulfur isotope records of the evolving Paleozoic marine sulfur reservoir. *Palaeogeogr. Palaeoclimatol. Palaeoecol.* **256**, 156–173.

Gill B. C., Lyons T. W. and Frank T. D. (2008) Behavior of carbonate-associated sulfate during meteoric diagenesis and implications for the sulfur isotope paleoproxy. *Geochim. Cosmochim. Acta* **72**, 4699–4711.

Hammarlund E. U., Dahl T. W., Harper D. A. T., Bond D. P. G., Nielsen A. T., Bjerrum C. J., Schovsbo N. H., Schönlaub H. P., Zalasiewicz J. A. and Canfield D. E. (2012) A sulfidic driver for the end-Ordovician mass extinction. *Earth Planet. Sci. Lett.* **331–332**, 128–139.

Helz G. R., Miller C. V., Charnock J. M., Mosselmans J. F. W., Pattrick R. A. D., Garner C. D. and Vaughan D. J. (1996) Mechanism of molybdenum removal from the sea and its concentration in black shales: EXAFS evidence. *Geochim. Cosmochim. Acta* **60**, 3631–3642.

Helz G. R., Bura-Nakic E., Mikac N. and Ciglenecki I. (2011) New model for molybdenum behavior in euxinic waters. *Chem. Geol.* **284**, 323–332.

Higgins J. A., Fischer W. W. and Schrag D. P. (2009) Oxygenation of the ocean and sediments: consequences for the seafloor carbonate factory. *Earth Planet. Sci. Lett.* **284**, 25–33.

Holland H. D. (2006) The oxygenation of the atmosphere and oceans. *Philos. Trans. R. Soc. B* **361**, 903–915.

Irwin H., Curtis C. and Coleman M. (1977) Isotopic evidence for source of diagenetic carbonates formed during burial of organic-rich sediments. *Nature* **269**, 209–213.

Isley A. E. and Abbott D. H. (1999) Plume-related mafic volcanism and the deposition of banded iron formation. *J. Geophys. Res.* **104**, 15461–15477.

Jin C., Li C., Peng X., Cui H., Shi W., Zhang Z., Luo G. and Xie S. (2014) Spatiotemporal variability of ocean chemistry in the early Cambrian, South China. *Sci. China Earth Sci.* **57**, 579–591.

Johnston D. T., Poulton S. W., Dehler C., Porter S., Husson J., Canfield D. E. and Knoll A. H. (2010) An emerging picture of Neoproterozoic ocean chemistry: insights from the Chuar Group, Grand Canyon, USA. *Earth Planet. Sci. Lett.* **290**, 64–73.

Johnston D. T., Poulton S. W., Tosca N. J., O'Brien T., Halverson G. P., Schrag D. P. and Macdonald F. A. (2013) Searching for an oxygenation event in the fossiliferous Ediacaran of northwestern Canada. *Chem. Geol.* **362**, 273–286.

Kah L. C., Lyons T. W. and Frank T. D. (2004) Low marine sulphate and protracted oxygenation of the Proterozoic biosphere. *Nature* **431**, 834–838.

Kendall B., Gordon G. W., Poulton S. W. and Anbar A. D. (2011) Molybdenum isotope constraints on the extent of late Paleoproterozoic ocean euxinia. *Earth Planet. Sci. Lett.* **307**, 450–460.

Kump L. R. and Seyfried W. E. (2005) Hydrothermal Fe fluxes during the Precambrian: effect of low oceanic sulfate concentrations and low hydrostatic pressure on the composition of black smokers. *Earth Planet. Sci. Lett.* **235**, 654–662.

Kusky T. M. and Li J. H. (2003) Paleoproterozoic tectonic evolution of the North China Craton. *J. Asian Earth Sci.* **22**, 383–397.

Li C., Love G. D., Lyons T. W., Fike D. A., Sessions A. L. and Chu X. (2010) A stratified redox model for the Ediacaran ocean. *Science* **328**, 80–83.

Li C., Love G. D., Lyons T. W., Scott C. T., Feng L. J., Huang J., Chang H. J., Zhang Q. R. and Chu X. L. (2012) Evidence for a redox stratified Cryogenian marine basin, Datangpo Formation, South China. *Earth Planet. Sci. Lett.* **331**, 246–256.

Li H. K., Su W. B., Zhou H. Y., Geng J. Z., Xiang Z. Q., Cui Y. R., Liu W. C. and Lu S. N. (2011) The base age of the Changchengian System at the northern North China Craton should be younger than 1670 Ma: constraints from zircon U–Pb LA-MC-ICPMS dating of a granite-porphyry dike in Miyun County, Beijing. *Earth Sci. Front.* **18**, 108–120.

Loyd S. J., Berelson W. M., Lyons T. W., Hammond D. E. and Corsetti F. A. (2012) Constraining pathways of microbial mediation for carbonate concretions of the Miocene Monterey Formation using carbonate-associated sulfate. *Geochim. Cosmochim. Acta* **78**, 77–98.

Lu S. N. and Li H. M. (1991) A precise U–Pb single zircon age determination for the volcanics of the Dahongyu Formation, Changcheng System in Jixian. *Bull. Chin. Acad. Geol. Sci.* **22**, 137–146.

Lyons T. W. and Severmann S. (2006) A critical look at iron paleoredox proxies: new insights from modern euxinic marine basins. *Geochim. Cosmochim. Acta* **70**, 5698–5722.

Lyons T. W., Werne J. P., Hollander D. J. and Murray R. W. (2003) Contrasting sulfur geochemistry and Fe/Al and Mo/Al ratios across the last oxic-to-anoxic transition in the Cariaco Basin, Venezuela. *Chem. Geol.* **195**, 131–157.

Lyons T. W., Reinhard C. T., Love G. D. and Xiao S. (2012) Geobiology of the Proterozoic Eon. In *Fundamentals of Geobiology* (eds. A. H. Knoll, D. E. Canfield and K. O. Konhauser). John Wiley & Sons Ltd, pp. 371–402.

Lyons T. W., Reinhard C. T. and Planavsky N. J. (2014) The rise of oxygen in Earth's early ocean and atmosphere. *Nature* **506**, 307–315.

Macdonald F. A., Strauss J. V., Sperling E. A., Halverson G. P., Narbonne G. M., Johnston D. T., Kunzmann M., Schrag D. P. and Higgins J. A. (2013) The stratigraphic relationship between the Shuram carbon isotope excursion, the oxygenation of Neoproterozoic oceans, and the first appearance of the Ediacara biota and bilaterian trace fossils in northwestern Canada. *Chem. Geol.* **362**, 250–272.

Meister P., McKenzie J. A., Vasconcelos C., Bernasconi S., Frank M., Gutjahr M. and Schrag D. P. (2007) Dolomite formation in the dynamic deep biosphere: results from the Peru Margin. *Sedimentology* **54**, 1007–1032.

Meng Q. R., Wei H. H., Qu Y. Q. and Ma S. X. (2011) Stratigraphic and sedimentary records of the rift to drift evolution of the northern North China craton at the Paleo- to Mesoproterozoic transition. *Gondwana Res.* **20**, 205–218.

Naehr T. H., Eichhubl P., Orphan V. J., Hovland M., Paull C. K., Ussler, III, W., Lorenson T. D. and Greene H. G. (2007) Authigenic carbonate formation at hydrocarbon seeps in continental margin sediments: a comparative study. *Deep Sea Res. Part II* **54**, 1268–1291.

Peng P., Liu F., Zhai M. G. and Guo J. H. (2012) Age of the Miyun dyke swarm: constraints on the maximum depositional age of the Changcheng System. *Chin. Sci. Bull.* **57**, 105–110.

Peng T., Bao H., Pratt L. M., Kaufman A. J., Jiang G., Boyd D., Wang Q., Zhou X., Yuan C., Xiao S. and Loyd S. (2014) Widespread contamination of carbonate-associated sulfate by present-day secondary atmospheric sulfate: evidence from triple oxygen isotopes. *Geology* **42**, 815–818.

Planavsky N. J., McGoldrick P., Scott C. T., Li C., Reinhard C. T., Kelly A. E., Chu X., Bekker A., Love G. D. and Lyons T. W. (2011) Widespread iron-rich conditions in the mid-Proterozoic ocean. *Nature* **477**, 448–451.

Planavsky N. J., Bekker A., Hofmann A., Owens J. D. and Lyons T. W. (2012) Sulfur record of rising and falling marine oxygen and sulfate levels during the Lomagundi Event. *Proc. Natl. Acad. Sci. USA* **109**, 18300–18305.

Planavsky N. J., Reinhard C. T., Wang X., Thomson D., McGoldrick P., Rainbird R. H., Johnson T., Fischer W. W. and Lyons T. W. (2014) Low Mid-Proterozoic atmospheric oxygen levels and the delayed rise of animals. *Science* **346**, 635–638.

Poulton S. W. and Canfield D. E. (2005) Development of a sequential extraction procedure for iron: implications for iron partitioning in continentally derived particulates. *Chem. Geol.* **214**, 209–221.

Poulton S. W. and Canfield D. E. (2011) Ferruginous conditions: a dominant feature of the ocean through Earth's history. *Elements* **7**, 107–112.

Poulton S. W. and Raiswell R. (2002) The low-temperature geochemical cycle of iron: from continental fluxes to marine sediment deposition. *Am. J. Sci.* **302**, 774–805.

Poulton S. W., Fralick P. W. and Canfield D. E. (2004) The transition to a sulphidic ocean ∼1.84 billion years ago. *Nature* **431**, 173–177.

Poulton S. W., Fralick P. W. and Canfield D. E. (2010) Spatial variability in oceanic redox structure 1.8 billion years ago. *Nat. Geosci.* **3**, 486–490.

Qiao X. F. (2002) Intraplate seismic belt and basin framework of Sino-Korean Plate in Proterozoic. *Earth Sci. Front.* **9**, 141–149.

Qiao X. F. and Gao L. Z. (2007) Mesoproterozoic paleoearthquake and paleogeography in Yan-Liao Aulacogen. *J. Palaeogeogr.* **9**, 337–352.

Raiswell R. and Canfield D. E. (1998) Sources of iron for pyrite formation in marine sediments. *Am. J. Sci.* **298**, 219–245.

Raiswell R., Newton R. and Wignall P. B. (2001) An indicator of water-column anoxia: resolution of biofacies variations in the Kimmeridge Clay (Upper Jurassic, UK). *J. Sediment. Res.* **71**, 286–294.

Raiswell R., Newton R., Bottrell S. H., Coburn P. M., Briggs D. E. G., Bond D. P. G. and Poulton S. W. (2008) Turbidite depositional influences on the diagenesis of Beecher's Trilobite Bed and the Hunsrück Slate; sites of soft tissue pyritization. *Am. J. Sci.* **308**, 105–129.

Reinhard C. T., Raiswell R., Scott C., Anbar A. D. and Lyons T. W. (2009) A late Archean sulfidic sea stimulated by early oxidative weathering of the continents. *Science* **326**, 713–716.

Reinhard C. T., Planavsky N. J., Robbins L. J., Partin C. A., Gill B. C., Lalonde S. V., Bekkerd A., Konhauser K. O. and Lyons T. W. (2013) Proterozoic ocean redox and biogeochemical stasis. *Proc. Natl. Acad. Sci. USA* **110**, 5357–5362.

Sadler P. M. (1981) Sediment accumulation rates and the completeness of stratigraphic sections. *J. Geol.* **89**, 569–584.

Scholz F., Severmann S., McManus J. and Hensen C. (2014) Beyond the Black Sea paradigm: the sedimentary fingerprint of an open-marine iron shuttle. *Geochim. Cosmochim. Acta* **127**, 368–380.

Schrag D. P., Higgins J. A., Macdonald F. A. and Johnston D. T. (2013) Authigenic carbonate and the history of the global carbon cycle. *Science* **339**, 540–543.

Scott C. and Lyons T. W. (2012) Contrasting molybdenum cycling and isotopic properties in euxinic versus non-euxinic sediments and sedimentary rocks: refining the paleoproxies. *Chem. Geol.* **324–325**, 19–27.

Scott C., Lyons T. W., Bekker A., Shen Y., Poulton S. W., Chu X. and Anbar A. D. (2008) Tracing the stepwise oxygenation of the Proterozoic ocean. *Nature* **452**, 456–459.

Scott C. T., Bekker A., Reinhard C. T., Schnetger B., Krapez B., Rumble, III, D. and Lyons T. W. (2011) Late Archean euxinic conditions before the rise of atmospheric oxygen. *Geology* **39**, 119–122.

Scott C., Wing B. A., Bekker A., Planavsky N. J., Medvedev P., Bates S. M., Yun M. and Lyons T. W. (2014) Pyrite multiple-sulfur isotope evidence for rapid expansion and contraction of the early Paleoproterozoic seawater sulfate reservoir. *Earth Planet. Sci. Lett.* **389**, 95–104.

Shen Y., Canfield D. E. and Knoll A. H. (2002) Middle Proterozoic ocean chemistry: evidence from the McArthur Basin, northern Australia. *Am. J. Sci.* **302**, 81–109.

Shen Y., Knoll A. H. and Walter M. R. (2003) Evidence for low sulphate and anoxia in a mid-Proterozoic marine basin. *Nature* **423**, 632–635.

Shi X., Jiang G., Zhang C., Gao L. and Liu J. (2008) Sand veins and MISS from the Mesoproterozoic black shale (ca. 1.7 Ga) in North China: implication for methane degassing from microbial mats. *Sci. China, Ser. D Earth Sci.* **51**, 1525–1536.

Slack J. F., Grenne T., Bekker A., Rouxel O. J. and Lindberg P. A. (2007) Suboxic deep seawater in the late Paleoproterozoic: evidence from hematitic chert and iron formation related to seafloor-hydrothermal sulfide deposits, central Arizona, USA. *Earth Planet. Sci. Lett.* **255**, 243–256.

Slack J. F., Grenne T. and Bekker A. (2009) Seafloor-hydrothermal Si–Fe–Mn exhalites in the Pecos greenstone belt, New Mexico, and the redox state of ca. 1720 Ma deep seawater. *Geosphere* **5**, 302–314.

Sperling E. A., Rooney A. D., Hays L., Sergeev V. N., Vorob'eva N. G., Sergeeva N. D., Selby D., Johnston D. T. and Knoll A.

H. (2014) Redox heterogeneity of subsurface waters in the Mesoproterozoic ocean. *Geobiology* **12**, 373–386.

Strauss H. (1993) The sulfur isotopic record of Precambrian sulfates: new data and a critical evaluation of the existing record. *Precambrian Res.* **63**, 225–246.

Taylor B. E., Wheeler M. C. and Nordstrom D. K. (1984) Isotope composition of sulphate in acid mine drainage as measure of bacterial oxidation. *Nature* **308**, 538–541.

Tromp T. K., Van Cappellen P. and Key R. M. (1995) A global model for early diagenesis of organic carbon and organic phosphorus in marine sediments. *Geochim. Cosmochim. Acta* **59**, 1259–1284.

Turekian K. K. and Wedepohl K. H. (1961) Distribution of the elements in some major units of the Earth's crust. *Geol. Soc. Am. Bull.* **72**, 175–191.

Wan Y. S., Zhang Q. D. and Song T. R. (2003) SHRIMP ages of detrital zircons from the Changcheng System in the Ming Tombs area Beijing: constraints on the protolith nature and maximum depositional age of the Mesoproterozoic cover of the North China Craton. *Chin. Sci. Bull.* **48**, 2500–2506.

Wilde P. (1987) Model of progressive ventilation of the late Precambrian-early Paleozoic ocean. *Am. J. Sci.* **287**, 442–459.

Wotte T., Shields-Zhou G. A. and Strauss H. (2012) Carbonate-associated sulfate: experimental comparisons of common extraction methods and recommendations toward a standard analytical protocol. *Chem. Geol.* **326**, 132–144.

Xu D. B., Wang D. Z., Bai Z. D., Mei M. X. and Li Z. Z. (2002) Sedimentary environment and facies model of the Mesoproterozoic Chuanlinggou Formation in the Xinglong area, Hebei. *Geol. China* **29**, 167–171.

Yan Y. Z. and Liu Z. L. (1998) The relationship between biocommunities and Paleoenvironments in Changcheng Period of the Yanshan Basin, North China. *Acta MicroPaleontol. Sin.* **15**, 249–266.

Zhang S., Li Z. X., Evan D. A. D., Wu H., Li H. and Dong J. (2012) Pre-Rodinia supercontinent Nuna shaping up: a global synthesis with new paleomagnetic results from North China. *Earth Planet. Sci. Lett.* **353–354**, 145–155.

Zhu Z., Aller R. C. and Mak J. (2002) Stable carbon isotope cycling in mobile coastal muds of Amapá, Brazil. *Cont. Shelf Res.* **22**, 2065–2079.

Associate editor: David Johnston